Mapping Dynamic Metabolic Energy Distribution in Brain Networks using fMRI: A Novel Dynamic Time Warping Framework

Sir-Lord Wiafe[1], Spencer Kinsey[1], Najme Soleimani[1], Raymond O. Nsafoa[2], Nigar Khasayeva[1], Amritha Harikumar[1], Robyn Miller[1*], Vince D. Calhoun[1]

[1]Tri-Institutional Center for Translational Research in Neuroimaging and Data Science (TReNDS), Georgia State University, Georgia Institute of Technology, and Emory University, Atlanta, GA 30303, USA. [2]Kwame Nkrumah University of Science and Technology (KNUST) Hospital, Kumasi, 00233, Ghana

Abstract

Understanding how metabolic energy is distributed across brain networks is essential for elucidating healthy brain function and neurological disorders. Research has established the link between blood flow changes and glucose metabolic processes that fuel neural activity. Here, we introduce a novel framework based on the normalized dynamic time warping algorithm robust to neural temporal variability, enabling reliable insights into metabolic energy demands using functional magnetic resonance imaging data. Our findings indicate that healthy brains maintain balanced energy distribution, whereas imbalances are more pronounced in schizophrenia with links to both positive and negative symptoms, particularly during rapid neural processes. Additionally, we identified a dynamic state that supports the brain criticality theory and is associated with higher-order cognitive abilities, demonstrating our framework's functional and clinical relevance. By linking metabolic energy distribution to neural dynamics, this framework provides a novel way to estimate and quantify the brain's maintenance of functional balance in a broadly applicable manner for studying brain health and disorders.

Keywords: brain energetics, dynamic time warping, high-frequency BOLD, brain criticality, schizophrenia

1. INTRODUCTION.

The human brain, despite constituting about 2% of the body's mass, consumes roughly 20% of its total energy[1]—a cost driven by intensive neuronal processing and synaptic activity essential for complex cognitive functions[2]. Functional magnetic resonance imaging (fMRI) leverages this metabolic demand by measuring the blood-oxygenation-level-dependent (BOLD) signal, which indirectly reflects neural activity through changes in cerebral blood flow and oxygenation[2,3]. The detectability of the BOLD signal arises from the retention of oxygen in the increased blood flow, underscoring glucose as the primary energy source for neurons[2]. Prior studies have shown that changes in blood flow are accompanied by comparable changes in glucose metabolism[4,5], making BOLD signal amplitude a reliable proxy for energy demand[4].

In contrast, techniques like positron emission tomography (PET) and magnetic resonance spectroscopy provide more direct insights into metabolism, but they lack the temporal resolution to capture rapid neural dynamics. Moreover, BOLD signal interpretation is complicated by variability in hemodynamics and neurovascular coupling (NVC), which introduce temporal lags and distortions[6], as well as the varying temporal scales of neural processing[7]. Commonly used measures such as the amplitude of low-frequency fluctuations (ALFF)[8], fractional ALFF[9], and dynamic ALFF[10] quantify BOLD signal power but do not account for temporal deformations, which may mask amplitude variations that are critical to assessing neural energy consumption. Similarly, prevalent dynamic functional connectivity measures—such as sliding window Pearson correlation[11], Hidden Markov Models[12], phase synchronization[13], wavelet coherence[14], and lagged cross-correlation[15]— primarily focus on synchronization and are amplitude scale invariant due to normalization procedures. Even many advanced deep learning models[16,17], including spatiotemporal models[18] struggle to fully capture these temporal dynamics.

There is therefore a pressing need for methodologies that can address both temporal misalignments and amplitude variations in BOLD signals to accurately reflect energy demand mismatches between neural networks. To this end, we propose leveraging dynamic time warping (DTW) to realign BOLD signal pairs, effectively mitigating temporal misalignments caused by hemodynamic variability and variable temporal scales. DTW is a time-series alignment technique that non-linearly warps the temporal dimension to align signals[19], allowing us to focus on the amplitude differences between the aligned signals. By analyzing BOLD signals in a way that compensates for temporal variability and hemodynamic delays, these amplitude differences indirectly estimate metabolic energy mismatch between neural networks. Specifically, DTW sums the aligned amplitude differences, and our recently proposed normalized DTW (nDTW)[20] computes the average of these differences, aligning with traditional signal energy and power computations respectively, as demonstrated in our study.

DTW has been introduced in fMRI studies as an alternative measure of functional connectivity[21], demonstrating benefits such as increased sensitivity to motor brain function[22], robustness to noise[21], higher test-retest reliability[21,22], and global signal regression robustness[21,22] compared to conventional correlation methods. DTW has also been effective in detecting group differences, including sex differences[21] and clinical disorders like schizophrenia[20] and autism spectrum disorders[22]. In our previous work, we expanded DTW's application by developing a novel warp elasticity measure, which leverages the alignment function from DTW to capture relative BOLD signal activation speeds (stretching and shrinking temporal dynamics) between networks[23,24]. These findings underscore the value of DTW in neuroimaging analyses.

In this study, we build on these findings by demonstrating that DTW-aligned amplitude differences serve as an effective metric for capturing activation amplitude discrepancies in the presence of temporal deformations. We incorporate a parameterization of the DTW cost function with a gamma parameter that emphasizes different scales of amplitude disparity—where higher gamma values accentuate larger amplitude differences and lower values highlight smaller ones[25]—to create a flexible framework for assessing metabolic energy demand mismatches across varying amplitude scales in the BOLD signal. Our focus is on resting-state fMRI (rs-fMRI) data, recognizing that significant energy is consumed even at rest and that resting-state activity is linked to metabolic processes[26].

The proposed two-cell model presents a unifying hypothesis that links schizophrenia to dysregulated glucose metabolism in astrocytes and neurons, suggesting that cognitive and psychiatric symptoms arise through a two-hit mechanism[27]. This hypothesis is supported by numerous studies connecting schizophrenia to disruptions in metabolic energy[28,29]. Based on this and recognizing that blood flow—carrying glucose—increases in response to higher energy demand, we investigate imbalances in energy demand between neural networks in individuals with schizophrenia compared to healthy controls using blood flow fMRI data. Consistent with previous findings, we focus on nDTW due to its increased sensitivity to group differences[20]. We hypothesize that energy mismatches between networks are more pronounced in broadband signals; therefore, we extend our analysis beyond the classic low-frequency BOLD signals to include higher frequency bands—specifically slow-5 (0.01–0.027 Hz), slow-4 (0.027–0.073 Hz), and slow-3 (0.073–0.198 Hz)—which have been shown to exhibit functional relevance[30]. We refer to the broader frequency ranges of 0.01–0.198 Hz and 0.01–0.15 Hz as F1 and F2, respectively. In addition, we develop a time-resolved nDTW measure to track how brain networks converge or diverge in their metabolic energy demands over time during rest.

By capturing these nuances, our approach offers a novel framework to understand neural network specialization and energy demand dynamics, with the potential to advance the characterization of neuropsychiatric disorders linked to energy metabolism abnormalities. This methodology not only enhances our ability to detect subtle energy imbalances within and between neural networks but also provides new insights into the pathophysiology of conditions such as schizophrenia with the potential to inform more targeted therapeutic interventions.

2. RESULTS

2.1. Simulation of DTW sensitivity non-stationarity and signal bandwidth

We evaluated DTW as a potential measure of metabolic energy demand mismatch between brain networks through simulations assessing its ability to detect amplitude disparities and its invariance to phase shifts. Sinusoids with varying amplitude and phase modulations were generated, and the performance of DTW, nDTW, and correlation was compared across different γ values and signal bandwidths (Supplementary Material).

DTW aligned original and temporally warped signals, demonstrating its capability to capture temporal deformations (Fig. 1a). Both DTW and nDTW remained invariant to non-stationary phase perturbations across increasing modulation indexes. In contrast, correlation decreased with higher phase modulation (Fig. 1b). In contrast, under non-stationary amplitude perturbations, correlation remained stable, while DTW and nDTW detected increasing amplitude disparities as modulation indexes rose (Fig. 1b).

The sensitivity of DTW and nDTW to amplitude scales was further examined by varying the γ parameter. Simulations involving amplitude non-stationarity across several modulation indexes revealed that smaller γ values resulted in higher rates of change in DTW and nDTW similarity scores at lower modulation indexes, indicating enhanced detection of minor amplitude disparities (Fig. 1c). Conversely, larger γ values exhibited higher rates of change at higher modulation indexes, reflecting improved tracking of substantial amplitude disparities (Fig. 1c). Additionally, while DTW generally maintains phase invariance, nDTW demonstrated slight sensitivity to phase differences when $\gamma \geq 1$ (Fig. 1c). This suggests that nDTW is better capable of responding to phase variations alongside amplitude tracking, offering a more nuanced assessment when absolute phase invariance is not essential.

In bandwidth analyses, DTW and nDTW sensitivity to randomness increased with broader full frequency spectrum, approaching the Nyquist frequency, unlike correlation, which remained unaffected (Fig. 1d). This indicates that amplitude differences become more prominent in broader full frequency bands.

Figure 1e illustrates nDTW ($\gamma = 1$) in capturing average aligned amplitude differences between brain networks. Lower nDTW values indicate convergence, potentially reflecting balanced metabolic energy demands, while higher values signify divergence, potentially highlighting greater energy demand discrepancies between networks (Fig. 1e).

Fig. 1: Simulation to analyze non-stationarity and signal bandwidth

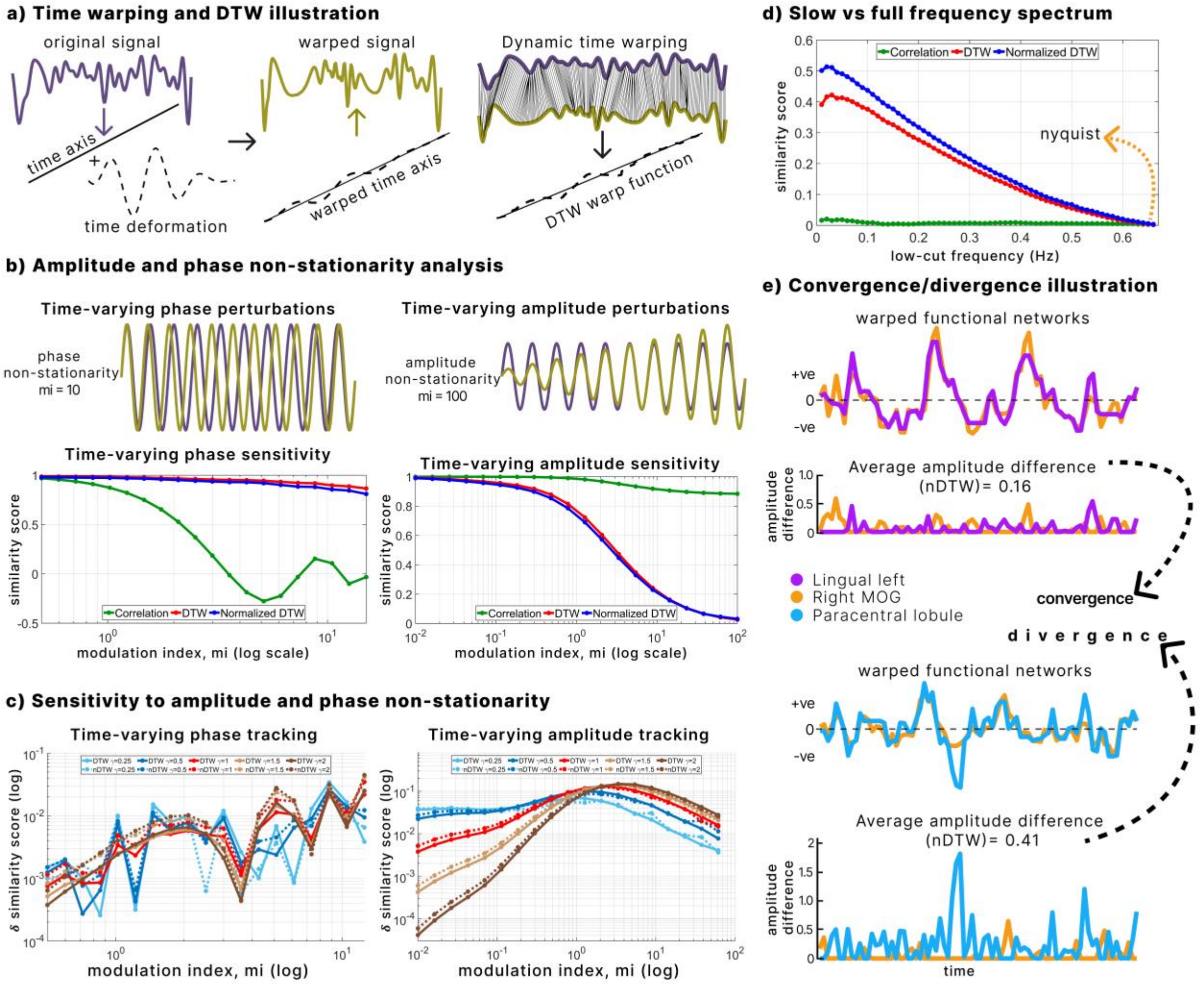

a. Illustration of DTW's ability to extract temporal deformations. A signal is warped by applying a modulation function (warp function) to its time index, and DTW successfully aligns the original and warped signals, extracting the induced temporal deformation. **b.** Behavior of DTW, nDTW and correlation under amplitude and phase non-stationarity. Time-varying amplitude perturbations (mi=100) and phase perturbations (mi=10) are shown. Similarity scores are derived from DTW and nDTW to highlight high distances (approaching 0) and low distances (approaching 1). Correlation is used as a benchmark. DTW and nDTW tracks amplitude disparities but remains invariant to phase shifts, unlike correlation. Both DTW and nDTW track amplitude disparities as mi increases (Time-varying amplitude sensitivity) but remain invariant to phase shifts, unlike correlation (Time-varying phase sensitivity). **c.** Sensitivity of DTW and nDTW to γ values in amplitude and phase non-stationarity. The derivative of similarity scores under amplitude non-stationarity reveals that for lower mi, smaller γ values yield higher scores compared to larger γ values, whereas for higher *mi*, larger γ values yield higher scores (Time-varying amplitude tracking). This indicates that smaller γ values are more adept at tracking minor amplitude disparities, while larger γ values are more suited to tracking larger amplitude disparities. Although DTW is inherently phase-invariant, nDTW exhibits slightly higher derivatives indication slight sensitivity to phase differences when $\gamma \geq 1$ (Time-varying phase tracking). **d.** DTW sensitivity across signal bandwidths. Random signal pairs (i.i.d Gaussian, $\mathcal{N}(0,1)$) are filtered with increasing bandwidths up to the Nyquist frequency. DTW alignment and distances demonstrate increasing sensitivity to disparities in broadband signals, unlike correlation, which remains unaffected by the increasing frequency spectrum. This highlights DTW's suitability for capturing disparities in full spectrum signals against slow narrowband ones. **e.** Illustration of convergence and divergence in brain networks. Using nDTW with $\gamma = 1$, the average amplitude difference between two pairs of aligned brain networks is shown. A small nDTW indicates convergence, while a large nDTW signifies divergence in signal power differences, providing insights into imbalances in metabolic energy demand.

2.2. Signal power imbalances between schizophrenia and control in broader fMRI bandwidth using nDTW

The intrinsic brain networks identified using the NeuroMark pipeline were categorized into seven domains: subcortical (SC), auditory (Aud), sensory motor (SM), visual (Vis), cognitive control (CC), default mode (DM), and cerebellum (Cb).

To validate the use of nDTW in the context of higher frequency fMRI data, we extended our analysis to include broader frequency bands (slow-5, slow-4, and slow-3; 0.01–0.198 Hz). We also examined the impact of varying γ values on test–retest reliability and sensitivity to group differences.

Focusing on the F1 frequency range, we observed that test–retest reliability improved with higher γ values, as indicated by lower mean ranks (Fig. 2a). γ values of ≥1.5 demonstrated significantly higher reliability compared to correlation after false discovery rate (FDR) (Wilcoxon signed-rank test, FDR corrected $p < 0.05$). Given that physiological noise correction in the fMRI data reduces within-subject variability[31], thus increasing test-retest reliability, the higher test-retest score for higher γ values may be indicative of the reduced sensitivity of higher γ values to physiological noise in the data.

Figure 2b illustrates that γ values of 1.5 and 1.25 exhibit the highest sensitivity for detecting group differences across both frequency ranges, outperforming other γ values and correlation. These γ values outperform other parameters and the correlation benchmark, as indicated by the greater number of directional arrows pointing towards them and the significant sensitivity enhancements marked by yellow asterisks. However, since $\gamma = 1.25$ has significantly lower test–retest reliability than the correlation benchmark (Fig. 2a), $\gamma = 1.5$ was selected as the optimal parameter for further analysis. Additionally, nDTW consistently detected more group differences in the broader F1 frequency range than in F2 across all γ values, whereas correlation did not. This indicates that nDTW is more sensitive to capturing clinical functional relevance at higher BOLD signal frequencies while maintaining high test–retest reliability, particularly at $\gamma = 1.5$.

Figure 2c shows that controls (lower triangle) consistently exhibit higher convergence in signal power differences, whereas individuals with schizophrenia (upper triangle) display greater divergence across several brain network pairs. This suggests that controls have more balanced metabolic energy demands between brain networks, while schizophrenia patients exhibit imbalances. Controls display significantly more convergent power differences than schizophrenia patients across multiple network pairs (positive red cells in the upper triangle of the FDR-corrected group difference matrix, Fig. 2c). Additionally, Cohen's d effect sizes (min-max = $0.19 - 0.89$; median = 0.49) highlight the practical significance of these group differences.

Furthermore, significant associations between nDTW scores and PANSS scores were identified. Positive PANSS associations were primarily observed between Cb networks and the DM, CC, and superior temporal gyrus (Aud), Vis and SC networks. In contrast, negative PANSS was mainly associated with connections between the CC, DM, and Vis brain networks.

Fig. 2: Reliability and group difference sensitivity across γ values and frequency bands

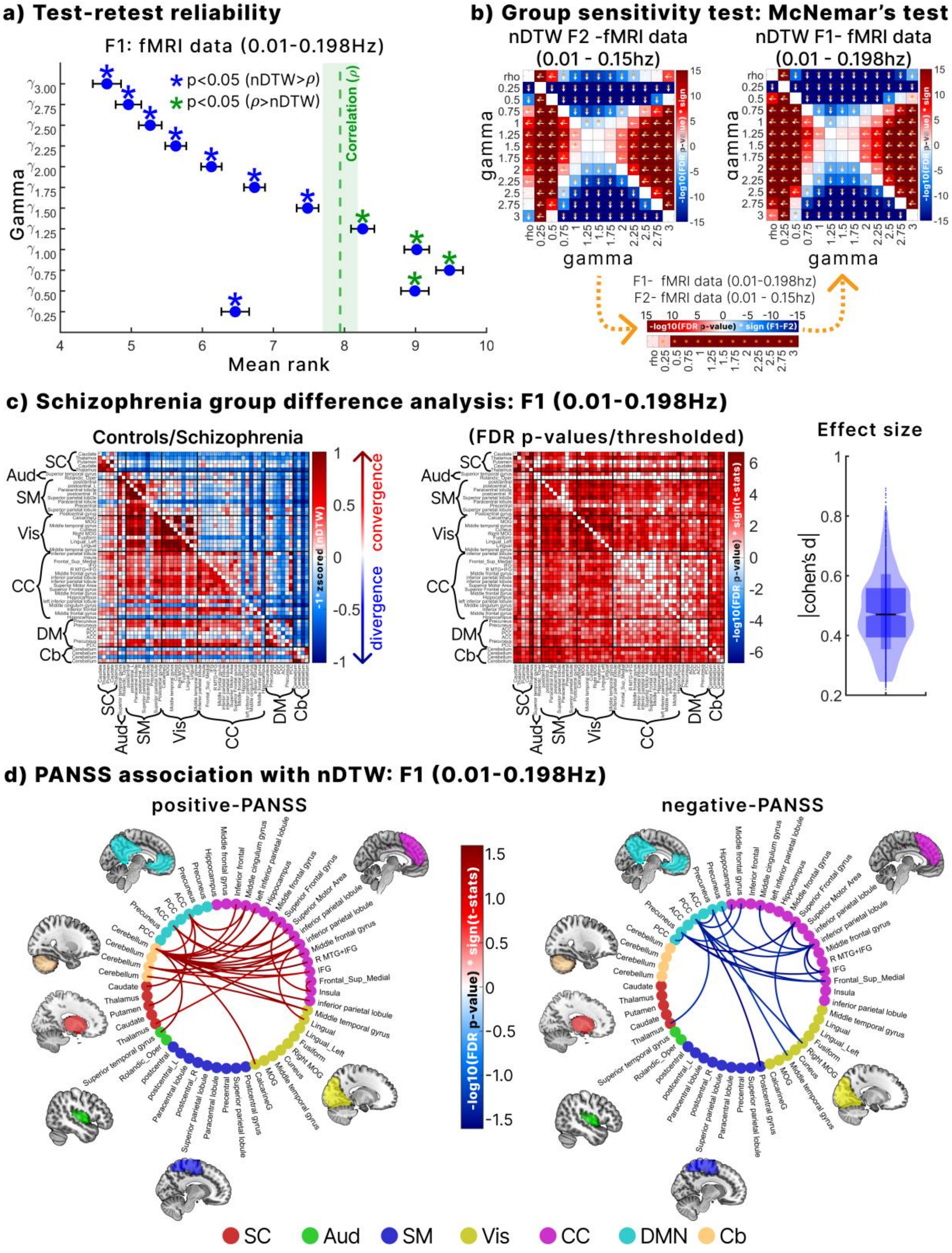

a. Test-retest reliability of nDTW was evaluated across multiple γ values using the HCP dataset, with correlation serving as a benchmark. The mean ranks for all twelve γ values and correlation are presented for the F1 frequency range. Lower mean rank values indicate higher test-retest reliability. γ values ≥ 1.5 and $\gamma = 0.25$ show significantly higher test-retest than correlation, as determined by a Wilcoxon signed-rank test (FDR-corrected p < 0.05) on the test–retest ranks. **b.** Gamma sensitivity in distinguishing schizophrenia from controls. We applied McNemar tests across all γ values for the F1 and F2 frequency ranges, as well as between F1 and F2. In the resulting matrices, arrows point to the parameter with higher sensitivity, and yellow asterisks highlight significant results with FDR-corrected p-values < 0.05. Results showed that γ values of 1.5 and 1.25 are the most effective in distinguishing schizophrenia patients from controls compared to other γ values and correlation for both F1 and F2 frequency ranges. Furthermore, the comparison between F1 and F2 demonstrates that all γ values increase group difference sensitivity when transitioning from F1 to F2, whereas correlation (rho) does not. These findings suggest that nDTW is more sensitive to group differences when higher frequencies are incorporated. **c.** Group difference between schizophrenia and controls using a $\gamma = 1.5$. nDTW values were z-scored across both groups and multiplied by -1, converting smaller nDTW values to positive scores (indicating convergence) and larger values to negative scores (indicating divergence). Group averages of nDTW scores reveal that controls exhibit convergence (lower triangle) while individuals with schizophrenia show divergence (upper triangle) across several brain network pairs. FDR-corrected p-values from a generalized linear model, controlling for sex, age, site, and mean frame displacement, are displayed in the lower triangle, with significant results (FDR < 0.05) highlighted in the upper triangle. The findings indicate that multiple brain network pairs show significant differences, with controls consistently demonstrating greater convergence than schizophrenia patients. Additionally, Cohen's d effect sizes exceeding 0.2 underscore the practical relevance of these group differences. **d** Association of nDTW with PANSS scores. Significant associations between brain network pairs and both positive and negative PANSS scores (FDR-corrected p < 0.05) were identified using a generalized linear model with a Poisson distribution. The analysis controlled for sex, age, site, and mean frame displacement. These significant associations are displayed for both positive and negative PANSS, highlighting the relationship between nDTW scores and symptom severity in schizophrenia.

2.3. Signal power imbalance effects of including higher frequency fMRI

We evaluated the effect of nDTW on expanding the frequency range from F2 to F1 by conducting paired sample t-tests for controls and individuals with schizophrenia separately. Normality of nDTW scores was confirmed using Shapiro-Wilk tests with t-values close to 1 across brain network pairs (Fig. 3a). After FDR correction, controls exhibited significantly increased convergence in F1 compared to F2, whereas schizophrenia patients showed greater divergence in F1 versus F2 across specific brain network pairs. These results suggest that broader F1 frequencies enhance metabolic energy balance in controls but exacerbate imbalances in schizophrenia, indicating that higher frequency fMRI enhances the identification of schizophrenia characteristics.

Cohen's d effect sizes were modest (median d = 0.18 for controls and d = 0.15 for schizophrenia). Nonetheless, higher frequencies amplified group distinctions, as reflected by larger effect size differences between controls and schizophrenia across several brain network pairs (Fig. 3a). Upset plot analysis identified 914 significant pairs across both frequencies, with 196 unique to F1 and 10 unique to F2, highlighting the enhanced group sensitivity of nDTW in F1 (Fig. 3b).

Figure 3b displays FDR-corrected p-values for significant pairs shared by both frequencies (left panel), with F1 (lower triangle) showing higher practical relevance than

F2 (upper triangle) based on effect sizes. Pairs unique to F1 had Cohen’s d > 0.2, underscoring nDTW's increased sensitivity and clinical relevance at higher frequencies.

To validate F1-unique pairs, we conducted null hypothesis testing using 1,000 surrogate datasets generated through phase randomization within the 0.15–0.198 Hz range (Fig. 3c). Several network pairs remained significant, confirming that higher frequency fMRI results are statistically robust and potentially derived from non-stationary amplitude processes.

Finally, we examined PANSS associations exclusively linked to F1 and not F2. Positive PANSS correlated with connections between the Cb with SC, DM, CC, Aud and Vis networks. Negative PANSS was primarily associated with CC-DM connections. These associations were absent in F2, suggesting that higher frequency fMRI enhances symptom severity detection.

Fig. 3: Clinical significance of high frequency fMRI data inclusion.

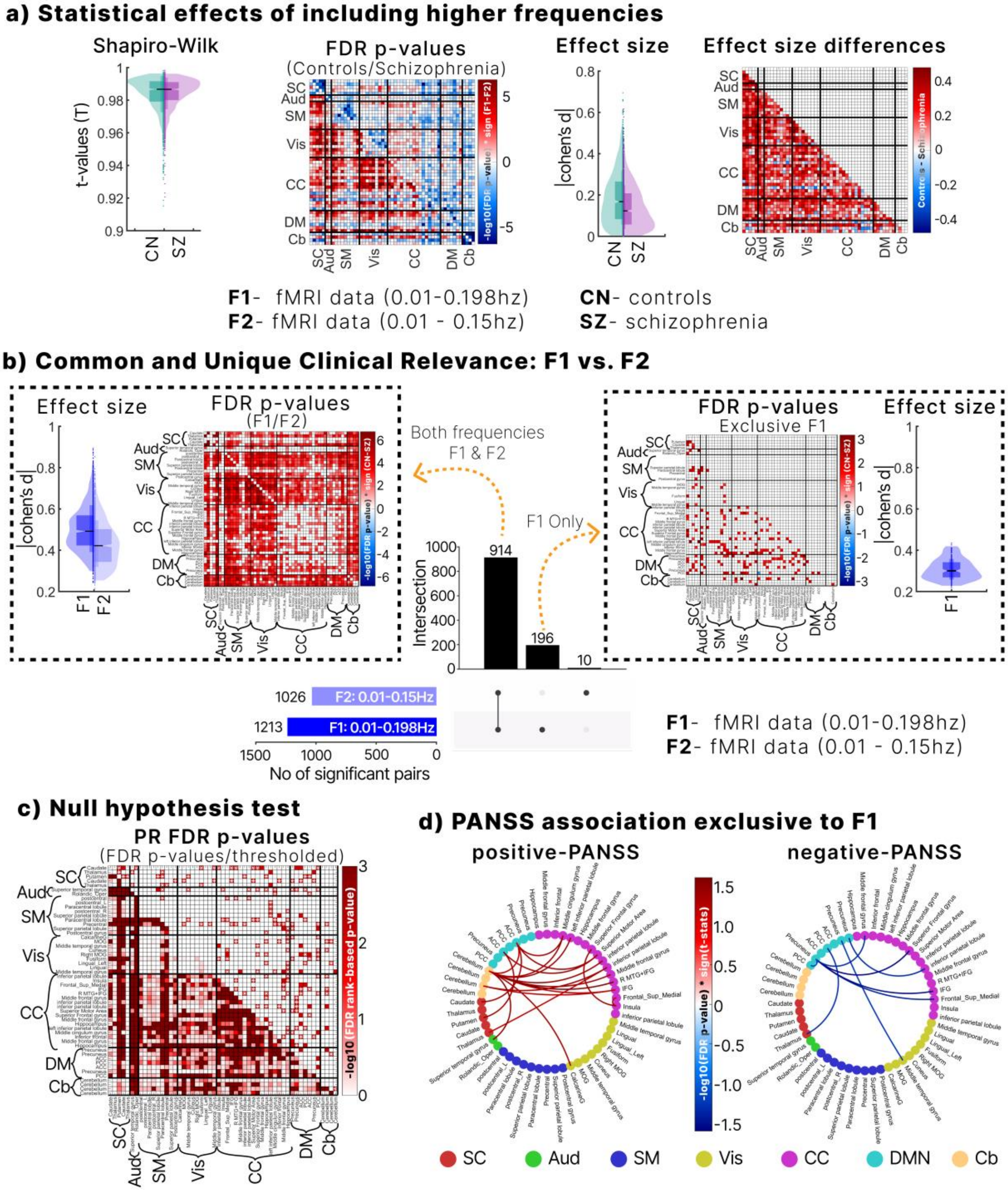

213

a. Statistical analysis of power imbalances between F1 and F2 frequencies. Shapiro-Wilk tests confirmed normality ($T\text{-}values \approx 1$) for all groups, validating the use of paired t-tests. FDR-corrected p-values of paired t-test indicated that controls exhibit increased signal power convergence, whereas individuals with schizophrenia show power divergence when transitioning from F2 to F1. This suggests that controls demonstrate greater convergence, while schizophrenia patients exhibit increased divergence with the inclusion of higher frequencies. Cohen's d effect sizes (~0.4) highlight enhanced separability between groups. **b.** Group differences from a generalized linear model controlling for sex, age, mean frame displacement, and site. FDR-corrected p-values across brain network pairs revealed 914 common significant pairs, with F1 showing larger effect sizes and greater practical relevance (left panel). Additionally, 196 significant pairs were uniquely identified in F1 with effect sizes above 0.2 (right panel), indicating modest practical relevance, while only 10 pairs were unique to F2. **c.** Null hypothesis testing using phase randomization confirmed that the significant brain network pairs uniquely identified in F1 are statistically relevant. **d.** Associations between normalized nDTW and PANSS scores were exclusively observed in the F1 frequency range, with no significant associations found in F2.

2.4. Dynamics of time-resolved nDTW

To identify recurring states of power imbalance dynamics, we applied k-means clustering with three clusters on the time-resolved nDTW, including both controls and individuals with schizophrenia. An elbow plot (Fig. 4c) confirmed that three clusters were optimal, determined by the derivative of the within-sum of squared distances. For visualization, we subtracted the median of all clusters and multiplied the distribution by -1, ensuring positive values represent convergence and negative values indicate divergence (Fig. 4a). The clusters were classified as follows: state 1—a convergent state, state 3—a divergent state, and state 2—a mixed state showing neither strong convergence nor divergence.

Figure 4b illustrates brain network representations for each state. In convergent state 1, the top 5% most convergent pairs predominantly involved sensory networks, including Vis, SM, and Aud networks. The divergent state 3 featured the top 5% most divergent pairs, mainly between the Cb and other networks. The mixed state 2 showed the top 2.5% most convergent and top 2.5% most divergent pairs, combining both dynamics.

A Markov chain was constructed to model state transitions, with transition probabilities shown in Figure 4d. Mixed state 2 had the highest self-retention probability (0.9021), followed by the convergent state 1 (0.8485) and divergent state 3 (0.8133). No direct transitions occurred between divergent and convergent states, likely due to the monotonicity constraint in the DTW alignment process, which prevents abrupt shifts without intermediate states.

The Markov chain's "stable point" (stationary distribution: Fig. 4e) showed that mixed state 2 accounted for 57.36% of system dynamics, the convergent state 1 for 37.21%, and the divergent state 3 for 5.42%. This highlights the predominance of mixed and convergent states in stabilizing power imbalance dynamics.

We further analyzed these dynamics by calculating the entropy rate and the convergence rate to the stationary distribution. The entropy rate was 36.6%, where 100% represents complete randomness and 0% indicates full order. This suggests a balance between randomness and order, with a slight preference for order (Fig. 4f). The rate of convergence computed by the spectral gap was 0.1851, and the mixing time—defined as the number of timesteps required to reach a tolerance level of 10^{-3} from the stationary distribution—was 36 timesteps (72 seconds; TR=2). The mixing time was determined from the farthest distribution point in the Markov chain's state space, specifically the state [0, 0, 1] (completely divergent), as shown in Fig. 4e.

We explored the relationship between entropy and convergence rate and investigated potential interventions to accelerate convergence and enhance cognitive ability by introducing perturbations to each transition probability and measuring the relative changes in convergence and entropy rates (Fig. 4g–h). Increasing self-retention in any brain state led to reductions in both convergence rate and entropy rate. While adding transitions between the mixed state and other states (excluding mixed to divergent) enhanced both rates, transitions between divergent and convergent states were marked with red crosses due to their impracticality as no such transitions were identified in the dynamics (Fig. 4d).

Notably, increasing transition probability from mixed to divergent states extends trajectories away from the stable point (Fig. 4e), reducing convergence speed. While this increased entropy, our findings suggest that higher entropy does not universally accelerate convergence; instead, the effect depends on the specific dynamic transitions within the Markov chain's state space.

Fig. 4: Dynamics of time-resolved nDTW

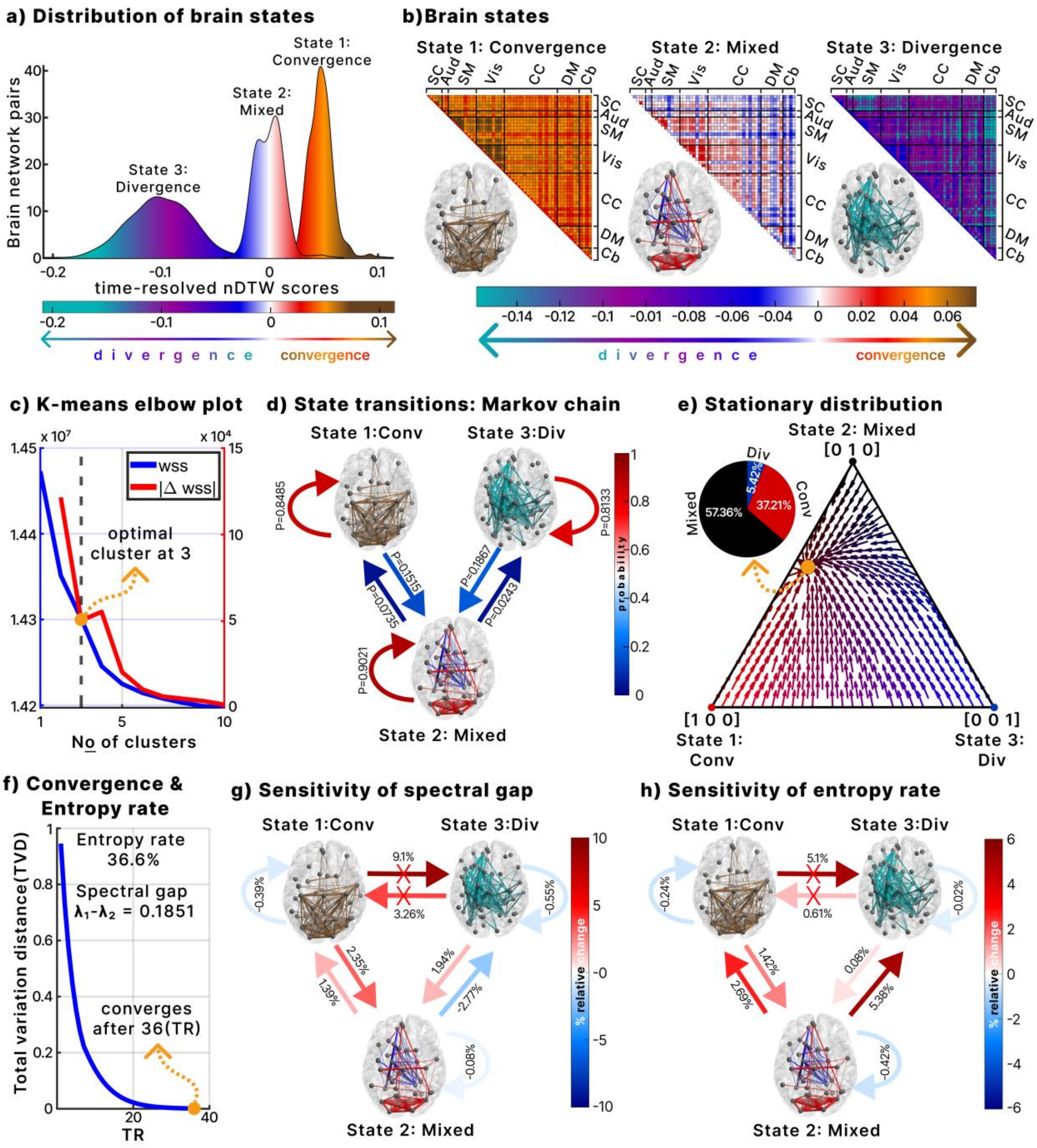

a. Distribution of recurring brain states identified using K-means clustering on time-resolved nDTW. The median across all 3 cluster centroids were subtracted and multiplied by –1 to ensure positive values represent convergence and negative values represent divergence. Three states were identified: convergent, divergent, and mixed. **b.** Brain state matrices with corresponding axial brain thumbnails. For convergent and divergent states, the top 5% most convergent and 5% most divergent brain connections are displayed, respectively. The mixed state shows the top 2.5% most convergent and top 2.5% most divergent connections. **c.** Elbow plot illustrating the within-sum of squared distances (WSS) for different cluster numbers. The first inflection point in the first derivative of WSS indicates that three clusters are optimal. **d.** State transition probabilities between the identified brain states, highlighting the likelihood of moving from one state to another. **e.** Stationary distribution within the Markov chain state space, demonstrating that the stable point of the dynamics is predominantly influenced by the mixed and convergent states. **f.** Mixing time of the dynamics, indicating the number of timesteps required to converge to the stationary distribution within a tolerance of 10^{-3}. Additionally, the convergence rate is shown through the spectral gap and entropy rate. **g.** Effects of perturbing state transitions on the spectral gap. Small perturbations were added to each transition probability, and the relative change in spectral gap was calculated to assess changes in convergence rate. **h.** Effects of perturbing state transitions on the entropy rate.

2.5. Group differences between controls and schizophrenia

We assessed group differences in metrics derived from time-resolved nDTW, including mean dwell time, occupancy rate, state transition probabilities, stationary distribution, spectral gap, mixing time, and entropy rate. Schizophrenia patients showed greater association with mixed state 2 and divergent state 3, while controls predominantly engaged with the convergent state 1. Specifically, schizophrenia patients had longer mean dwell times in mixed and divergent states, whereas controls spent more time in the convergent state (Fig. 5a). Similarly, occupancy rates (Fig. 5b) reflected higher mixed and divergent state occupancy in schizophrenia, and greater convergent state occupancy in controls.

The stationary distribution (Fig. 5d) revealed that schizophrenia dynamics are more influenced by mixed and divergent states than controls, while controls are more influenced by the convergent state than schizophrenia. State transition probabilities showed controls were more likely to transition from mixed to convergent states (Fig. 5c). In contrast, schizophrenia patients had increased transitions from convergent to mixed, mixed to divergent, and higher self-retention in both mixed and divergent states.

Fig. 5: Group differences and cognitive score associations

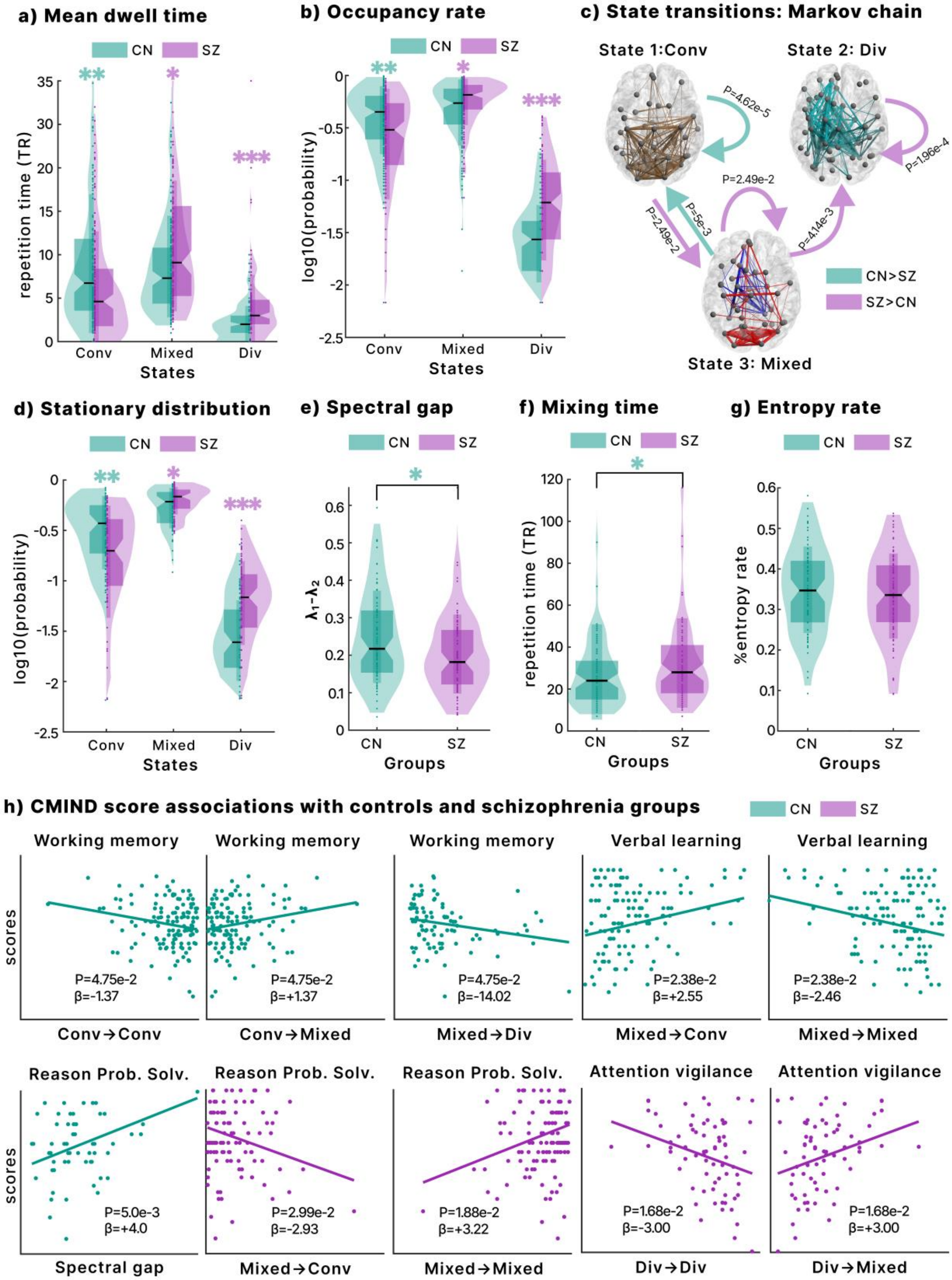

a. Mean dwell time in each state for schizophrenia patients and controls, highlighting increased dwell time in mixed and divergent states for schizophrenia and convergent state for controls**.** **b.** Occupancy rate of each state, showing longer occupancy in mixed and divergent states for schizophrenia and in convergent state for controls. **c.** State transition probabilities between states for schizophrenia patients and controls, illustrating higher transition rates from convergent to mixed and mixed to divergent states in schizophrenia. **d.** Group difference in stationary distribution of the Markov chain. **e.** Spectral gap, reflecting the convergence rate, is higher in controls compared to schizophrenia patients, suggesting faster convergence to the stable point in controls. **f.** Mixing time, representing the number of timesteps required to reach the stationary distribution within a tolerance of 10^{-3}, is shorter in controls than in schizophrenia patients, indicating quicker convergence in controls. **g**. Entropy rate, showing the balance between order and flexibility, does not differ significantly between groups. **h.** Associations between cognitive scores and nDTW metrics, analyzed separately for each group to account for group bias. In controls, working memory and verbal learning are associated with specific state transitions and spectral gap is associated with reasoning and problem-solving. In schizophrenia, reasoning, problem-solving, and attention vigilance are linked to different transitions and state retention.

All analyses were conducted using generalized linear models controlling for sex, age, site, and mean frame displacement. Results were FDR-corrected with a significance threshold of 0.05. One asterisk (*) indicates p-values between 0.05 and 0.01, two asterisks (**) indicate p-values between 0.01 and 0.001, and three asterisks (***) indicate p-values below 0.001.

Regarding convergence to the stationary distribution, controls exhibited a higher spectral gap, indicating a faster convergence rate (Fig. 5e). Using a tolerance of 10^{-3} and starting from the completely divergent state ([0, 0, 1]), controls also had a lower mixing time, reflecting quicker stabilization. No significant difference in entropy rate was observed, suggesting that faster convergence rates in controls may stem from dynamic transition efficiency rather than entropy.

2.6. Controls and schizophrenia cognitive score associations

We examined associations between time-resolved nDTW metrics and Computerized Multiphasic Interactive Neurocognitive System (CMINDS) scores using generalized linear models (GLM) for controls and schizophrenia patients separately to avoid group bias (Fig. 5h).

In controls, working memory was positively associated with transitions from convergent to mixed states and negatively associated with convergent self-retention and mixed-to-divergent transitions, indicating that transitions into the mixed state support memory performance. Verbal learning was positively associated with transitions from mixed to convergent states and negatively with convergent-to-mixed transitions, suggesting that the convergent state facilitates verbal learning. Additionally, the spectral gap was positively associated with reasoning and problem-solving, highlighting the link between faster convergence rates and higher cognitive performance.

In schizophrenia, reasoning and problem-solving were negatively associated with transitions from mixed to convergent states but positively with self-retention in the mixed state. Attention vigilance was positively associated with transitions from divergent to mixed states and negatively with self-retention in the divergent state. These results suggest that specific dynamic transitions, such as moving into the mixed state, enhance cognitive abilities in schizophrenia, whereas others, like remaining in the divergent state, may impede them.

3. DISCUSSION

This study developed a comprehensive framework to assess power imbalances between brain networks using fMRI data, offering insights into metabolic energy demands while accounting for varying temporal scales of brain activity. The physiological basis of the BOLD signal is not entirely straightforward. Studies combining fMRI with PET imaging have shown that the magnitude of the BOLD signal can track glucose utilization in the brain[4,5]. However, other studies indicate that even under conditions of hyperemia (excess amount of blood) and hyperoxia (excess amount of oxygen), the BOLD signal still accompanies neuronal activation, suggesting that it does not strictly reflect a deficiency of glucose or oxygen[32,33]. Research further supports this by proposing that due to the slow response of NVC, neurons initially rely on astrocytic glycogen and lactate stores before blood flow compensates for energy use[34,35]. This indicates that blood flow does not simply match real-time neuronal energy consumption[36]. Nevertheless, neuronal activation consistently triggers vasoactive signaling, leading to vasodilation through NVC, regardless of brain baseline oxygen or glucose levels[33]. Therefore, while the immediate energy source may vary, the magnitude of the BOLD signal consistently reflects the overall energy demand driven by neuronal activation, whether the energy is supplied by blood-derived glucose and oxygen or by intracellular reserves. Tracking amplitude changes in BOLD signals using DTW provides valuable insights into metabolic energy demands, offering robustness against temporal variability introduced by neural processing and hemodynamic modulations.

By utilizing our recently proposed nDTW metric[20], we explored functional relevance beyond the typical 0.01–0.15 Hz range. Our time-resolved nDTW identified three intuitive brain states: convergence, divergence, and a mixed state, indicating flexibility in energy distribution. Simulations confirmed the robustness of nDTW in capturing amplitude and power disparities between signals, tracking non-stationary amplitude changes, and remaining invariant to timing and phase deformations. Importantly, our framework demonstrated functional relevance by associating brain dynamics with clinical and cognitive scores.

Static results revealed that control subjects exhibited stronger convergence, while schizophrenia showed relatively greater divergence in brain network power disparities. Our static analysis suggests that healthy controls maintain more uniform energy demand across brain networks globally, whereas individuals with schizophrenia exhibit significant imbalances. These imbalances reflect abnormal glucose metabolic demands and align with existing studies demonstrating that schizophrenia is associated with glucose metabolism abnormalities, including an increased risk of diabetes and insulin resistance[37,38].

A key finding was the increased convergence in controls and increased divergence in schizophrenia when higher-frequency signals were included. These results indicate that high-frequency BOLD signals—indicating rapid glucose utilization—play a crucial role in supporting healthy cognition and enhancing the distinction between control subjects and those with schizophrenia. In controls, the inclusion of these frequencies appeared to increase the balance of metabolic energy demands across brain networks, while in schizophrenia, it exacerbates imbalances. Furthermore, several brain network pairs showed significant differences between controls and schizophrenia exclusively when higher frequencies were included. The phase-randomized null model confirmed that these results were statistically significant and likely attributable to non-stationary amplitude processes detected by nDTW. While synchronization studies have established the functional relevance of higher-frequency BOLD signals[30], our findings provide a novel perspective. We demonstrate that higher-frequency BOLD signals improve the distinction between control individuals and those with schizophrenia by capturing non-stationary energy demand disparity during rapid neural processing.

We also found positive associations between nDTW and positive symptoms, particularly in connections involving the cerebellum with the Aud, DM, CC, SC, and Vis domains. The cerebellum, recognized as a key predictive hub in the brain[39], not only regulates rapid cognitive processing—including speed, capacity, and consistency[40]— but also plays a central role in orchestrating mental coordination. This observation aligns with the “cognitive dysmetria” theory, which attributes schizophrenia to impaired coordination among prefrontal regions, thalamic nuclei, and the cerebellum[41].

Our findings further support this theory, revealing that altered cerebellar coordination of neural processing is linked with positive symptoms[41]. Specifically, lower divergence—or relatively higher convergence—in schizophrenia was correlated with more severe positive symptoms such as hallucinations, delusions, and disorganized thinking. Considering that our results show significantly stronger convergence in controls compared to individuals with schizophrenia, the observed positive associations with symptom severity may indicate maladaptive or compensatory [42] cerebellar coordination of glucose utilization, inadvertently exacerbating positive symptomatology in the affected networks.

Negative associations were observed between brain networks and negative symptoms, indicating that lower convergence (or higher divergence) is linked to more severe negative symptoms. These associations were most prominent between higher-order processing networks such as DM and CC. Given that negative symptoms—characterized by reduced motivation, pleasure, and emotional expression—are linked to high-level cognitive processing[43], our findings suggest that greater imbalances in metabolism demands within and between the DM and CC are associated with increased negative symptoms in schizophrenia. Prior studies have connected impaired metabolism to negative symptoms like depression[44,45], and a recent study found that improvements in glucose metabolism—achieved through prefrontal cortex stimulation—were associated with reductions in negative symptoms[46].

Notably, most of the PANSS associations identified were due to the inclusion of higher frequencies, emphasizing the importance of higher frequency BOLD signal. Although higher frequency bands have been associated with various sources of noise[47], work has also identified high frequency fluctuations as a source of non-noise variability[30,48,49]. Alterations within such frequency bands may therefore reflect alterations to rapid neural processing and rapid glucose utilization in schizophrenia.

Our framework identified three dynamic states: convergent, divergent, and mixed. The convergent state reflects relatively balanced energy demands, suggesting that neural circuits are operating within optimal ranges, with consistent glucose delivery supporting stable metabolism and neural energy homeostasis[50]. Conversely, the divergent state represents imbalanced energy demands, where certain brain networks receive either insufficient or excessive blood flow. This imbalance can destabilize neural activity and disrupt the homeostatic regulation of brain energy, ultimately leading to reduced cognitive performance[45,50,51]. The mixed state lies between these extremes, reflecting neither strong convergence nor strong divergence. Transitions were observed only between the mixed and either the convergent or divergent states, with no direct shifts between convergent and divergent states (Fig. 4d). Thus, the mixed state appears to function as an adaptive intermediary, enabling the brain to switch flexibly between functional states as needed.

The brain criticality theory posits that the brain functions near a critical point—a delicate balance between order and disorder[52]. The mixed state in our framework exemplifies this balance, contributing 57.36% to the stationary distribution. Combined with the Markov chain's entropy rate of 36.6%, this finding suggests that the brain operates closer to the critical entropy point of 50% rather than being too ordered or too disordered, with a slight bias toward order that remains within the “zone of criticality”[53]. Indeed, critical entropy serves as an indicator of brain criticality[54]—a state that helps the brain maintain flexibility and adaptability in its functions.

A key dynamic metric in our study is the convergence rate, which measures how quickly a system reaches its stable state. Our perturbation analysis revealed that increasing self-retention probabilities reduced both convergence and entropy rates. This is because higher self-retention enforces predictability, which runs counter to the flexibility required by criticality theory. Generally, higher convergence rates correlated with increased entropy, except for transitions from the mixed to divergent state—highlighting the significant role of transition dynamics in convergence. State space analysis further demonstrated that trajectories moving from the divergent state takes the longest to reach the stable point (Fig. 4e), thereby validating why increasing mixed to divergent transitions reduces the rate of convergence to the stable point. This pattern underscores the need to balance order and disorder (i.e., to increase entropy) while optimizing the trajectory toward stability.

Importantly, control subjects exhibited significantly higher convergence rates—evidenced by metrics such as the spectral gap and mixing time—compared to patients with schizophrenia, despite both groups maintaining similar entropy levels. This suggests that although both groups operate near critical entropy, the dynamics of schizophrenia hinder efficient convergence to stability, likely due to altered transition pathways. These findings further imply that high entropy does not necessarily equate to enhanced information integration or superior cognitive performance, challenging the notion that richer conscious experiences always result from increased entropy[55].

Cognitive flexibility was further underscored by the associations observed with the mixed state. In control subjects, working memory performance was positively linked to transitions from convergent to mixed states and negatively associated with both self-retention in the convergent state and transitions from mixed to divergent states. These relationships suggest that the mixed state—reflecting critical dynamics—facilitates the flexibility necessary for effective higher-order functions such as working memory[56]. In individuals with schizophrenia, reasoning and problem-solving abilities were negatively associated with transitions from mixed to convergent states, while showing positive associations with self-retention in the mixed state and transitions from divergent to mixed states. Additionally, attention vigilance was negatively related to self-retention in the divergent state but positively correlated with transitions from divergent to mixed states. Overall, these findings emphasize the pivotal role of the mixed state in supporting cognitive flexibility and indicate that disruptions in transitions to and from this state may contribute to the cognitive impairments observed in schizophrenia.

However, the mixed state may not be optimal for every task. For example, in control subjects, transitions from the mixed to convergent state were positively associated with verbal learning, whereas extended self-retention in the mixed state showed negative associations. Given findings that verbal learning benefits from structured cognitive training[57]—consistent with the ordered nature of the convergent state—it appears that while the mixed state promotes flexibility, tasks that require structured cognition may rely more on the consistency of the convergent state. Overall, these results underscore the importance of balancing flexibility and stability to optimize cognitive performance.

Group-level analysis revealed that controls predominantly engaged in the convergent state, while schizophrenia subjects showed greater involvement in the mixed and divergent states. Metrics such as mean dwell time, fraction rate, state transitions and stationary distribution confirmed these patterns. The increased presence of divergent states in schizophrenia aligns with the disorder’s characteristic disruption in neural dynamics[58]. Furthermore, as transitions toward the mixed state were found to decrease the convergence rate to stability, the excessive engagement of the mixed state in schizophrenia may reflect an overly sustained flexibility that potentially undermines cognitive processes such as working memory.

Although our study provides a unifying platform connecting various brain mechanistic concepts, the use of BOLD fMRI inherently reflects relative rather than absolute metabolic energy demands. Since BOLD is a hemodynamic signal rather than a direct measure of energy consumption, its amplitude does not correspond to absolute metabolic differences. Additionally, preprocessing steps such as z-scoring remove mean and variance information, making the signal inherently relative. Performing ICA further emphasizes this, as ICA focuses on maximizing statistical independence and extracting components based on relative differences rather than absolute amplitudes. As a result, while we cannot directly map differences in network amplitudes onto absolute physiological energy demands, relative changes over time in ICA signals remain meaningful and provide valuable insights into how different brain networks engage with varying levels of neural activity and associated metabolic demand.

In summary**,** we provide evidence to suggest that schizophrenia is characterized by a pronounced disparity in metabolic energy distribution across the brain, both throughout the scanning session and dynamically, becoming more evident during rapid neural processing. Additionally, we observed maladaptive metabolic energy demands in a hub-like interaction between the cerebellum and other brain networks linked to positive symptoms, while stronger heterogeneity in energy demands across high-order processing networks, such as the DM and CC, was associated with negative symptoms. Our findings provide a novel and intuitive perspective on brain criticality using blood flow, revealing that cognitive flexibility—a key marker of brain criticality—is linked to improved working memory and fluid intelligence in both controls and individuals with schizophrenia. However, we also establish that cognitive flexibility may hinder performance on structured tasks like verbal learning. Furthermore, transitions into a state of greater energy demand heterogeneity are associated with declines in attention and vigilance in schizophrenia. Finally, we propose a therapeutic intervention in Supplementary material using photobiomodulation and the developed directional DTW. This comprehensive framework linking blood flow to cognition and schizophrenia symptoms offers a unifying perspective for various hypotheses of brain function in neuroscience research.

4. METHODS

4.1. Dynamic time warping as a measure of energy/power disparity

Dynamic time warping is a widely used signal processing algorithm that aligns signals with nonlinear temporal deformations by applying adaptive “elastic” transformations to achieve a meaningful similarity measure[19,59]. When temporal deformations complicate phase or timing relationships, it becomes logical to isolate these aspects and concentrate solely on the amplitude of the signals. DTW tackles this by resolving temporal dissimilarities, optimally aligning signal pairs to minimize a distance metric and bring them to a shared temporal scale, leaving amplitude as the primary source of disparity.

The algorithm computes a distance cost matrix that captures the cumulative cost of aligning pairwise elements of the sequences and identifies the optimal warping function to adjust their time axes, minimizing a distance metric. To enhance computational efficiency and ensure meaningful alignments, particularly when guided by domain knowledge, a window size constraint is applied to limit the maximum allowable warping between indices in the time series[19].

For discrete signals x and y of lengths N and M respectively, the distance cost matrix, $CM_{DTW(i,j)}$, is initialized as follows:

$$CM_{DTW(i,j)\epsilon(x,y)} = \begin{cases} 0, if\ (i,j) = (0,0) \\ +\infty, otherwise \end{cases}$$

The cells in $CM_{DTW(i,j)}$ that are within the allowable window, w, can be defined as:

$$\begin{aligned} CM_{DTW(i_w,j_w)\epsilon\{|i-j|\leq w\}} \\ = \lambda_\gamma(x_{i_w}, y_{j_w}) \\ + min \begin{cases} CM_{DTW(i_w-1,j_w-1)} \\ CM_{DTW(i_w-1,j_w)} \\ CM_{DTW(i_w,j_w-1)} \end{cases} \end{aligned} \quad (1)$$

Following the parameterization of the DTW algorithm recently proposed[25], let $\gamma\epsilon\mathbb{R}^+$ denote that γ is a positive real number. Then, the generalized distance metric is given as:

$$\lambda_\gamma(x_{i_w}, y_{j_w}) = \left|x_{i_w} - y_{j_w}\right|^\gamma \quad (2)$$

Where $\gamma > 1$ emphasizes large amplitude disparity, $\gamma < 1$ highlights small amplitude disparity and $\gamma = 1$ provides a balance between both[25].

The optimal warping path or function φ, with length L, derived from DTW, is the path that belongs to the set of all possible warping functions Π, where the cumulative distance metric between corresponding points in signals x and y is minimized. It can be expressed as:

$$\varphi = \arg min_{\varphi\epsilon\Pi} \sum_{(i_w,j_w)\epsilon\{|i-j|\leq w\}} CM_{DTW(i_w,j_w)} \quad (3)$$

Where $L \geq \max\,(M, N)$

The distance cost D in DTW, which measures the phase/timing-invariant amplitude disparity between the signal pair, is computed as the sum of distance metric along the warping path. This cost is expressed as:

$$D = \sum_{\tau=1}^{L} CM_{DTW(\varphi_x(\tau),\varphi_y(\tau))} \qquad (4)$$

Where τ is the time index for the warp function, $\varphi_x(\tau)$ is the warping path along signal x, and $\varphi_y(\tau)$ is the warping path along signal y.

Notably, when the distance metric with $\gamma = 2$ is chosen the DTW distance cost becomes:

$$D = \sum_{\tau=1}^{L} \left| x(\varphi_x(\tau)) - y\left(\varphi_y(\tau)\right) \right|^{\gamma=2} \qquad (5)$$

This represents the energy of the difference signal $x(\varphi_x(\tau)) - y\left(\varphi_y(\tau)\right)$, with the normalized DTW [20] distance cost D_n, representing the power of the difference signal, as given below:

$$D_n = \frac{1}{L} \sum_{\tau=1}^{L} \left| x(\varphi_x(\tau)) - y\left(\varphi_y(\tau)\right) \right|^{\gamma=2} \qquad (6)$$

This positions the algorithm as a measure of temporal/phase-invariant energy/power disparity between two signals. Leveraging the $\gamma-$parameterization, DTW and nDTW effectively capture energy and power disparities between signals, respectively. This flexible framework adjusts to different amplitude scales based on the value of γ.

We define *convergence* as the scenario where the energy or power differences—quantified by DTW and nDTW respectively—are relatively low, indicating that the signal levels are close together. Conversely, when these differences are relatively high, we refer to it as *divergence*.

In the context of fMRI signals, convergence between two brain networks suggests that the metabolic energy demands, or consumption of the corresponding neural networks are homogenous. Conversely, divergence suggests an imbalance in energy demands between these networks. These patterns provide insights into the metabolic energy specificity and functional interactions of brain networks.

4.2. Allowable window size for fMRI application

The two main challenges of DTW are its computational cost, with a time complexity of $O(M \times N)$, and the issue of singularities[19], where a single time point in one signal is unnaturally matched to a large portion of the other signal. Both challenges are mitigated by constraining the alignment to a window size that limits the maximum window of allowable alignment[60]. Given the focus on temporal deformations such as leads/lags and nonlinear dynamics like stretching and shrinking, selecting an appropriate window size to capture relevant temporal deformations in fMRI data is crucial. In our previous study using the proposed warp elasticity approach, we demonstrated that stretching and shrinking dynamics could introduce anti-correlations[24]. Considering that anti-correlations may also arise from lead/lag relationships, it is intuitive to choose a window size that spans the length of the signal required to produce maximum anti-correlations (-1). This approach has also been validated as optimal in prior fMRI studies[21]. The longest wavelength yielding an anti-correlation of -1 corresponds to the lowest frequency component $(0.01Hz)$, which equates to a 100-second window. Achieving an anti-correlation of -1, requires a time shift of half the wavelength (50 seconds). For the DTW algorithm to capture relevant temporal deformations in fMRI data, two 50-second windows are sufficient to account for deformations in both directions, resulting in a total window length of 100 seconds[21], corresponding back to the low-cutoff frequency of $0.01Hz$. However, since the filter design for the data—commonly Butterworth—is typically nonideal, we instead recommend selecting a window size based on the spectral characteristics of the activity signal, determined by the $-3db$ point of the low-frequency cutoff of the fMRI signal[13,23,24,61]. The equation for determining the window size is:

$$f_{3db} = \frac{0.88}{\sqrt{N^2 - 1}} F_s \tag{7}$$

Where N represents the number of points in the window, F_s denotes the sampling frequency, and f_{3db} is the low cutoff frequency.

4.3. Time-resolved nDTW

To derive a time-resolved evolution of power imbalances between signals, we modify the nDTW measure by eliminating its summation and normalization components. This yields a time-resolved power mismatch metric, $D_{tr}(\tau)$, for the aligned signals, ensuring that its average corresponds to the original nDTW value. The formulations are as follows:

$$\begin{gathered} D_{tr}(\tau) = \left| x\left(\varphi_x(\tau)\right) - y\left(\varphi_y(\tau)\right) \right|^{\gamma} \\ D_n = \frac{1}{L} \sum_{\tau=1}^{L} D_{tr}(\tau) \end{gathered} \tag{8}$$

However, the DTW algorithm results in aligned signal lengths L that vary across different signal pairs, complicating comparisons between brain network pairs. To ensure that the length of the time-resolved metric equals the signal length and averages to the nDTW, it is necessary to interpolate $D_{tr}(\tau)$ with the warped time scale (τ) to have the same length as the original time index (t), N or M (noting that $N = M$). This interpolation must preserve the integrity of the metric, particularly the first derivatives of the warping functions, which are crucial for capturing the varying temporal scales of fMRI time series as established in our previous study[24].

To address this, we employed the piecewise cubic Hermite interpolating polynomial (PCHIP) method for interpolating $D_{tr}(\tau)$ to the original signal length N. PCHIP was selected for its ability to preserve the shape and monotonicity[62] of the original warping functions, thereby maintaining the temporal dynamics of the fMRI signals. Unlike standard cubic splines, PCHIP avoids introducing artificial oscillations and overshoots[62], ensuring the fidelity of the power mismatch measurements. Additionally, PCHIP guarantees continuous first derivatives[62], aligning with our requirement to maintain the derivatives of the warping functions. This interpolation ensures that the interpolated metric $D_{tr}^{pchip}(\tau)$ accurately averages to the D_n, facilitating consistent and comparable analyses across all brain network pairs.

The interpolated time-resolved nDTW metric is thus defined as:

$$D_{tr}^{pchip}(\tau) = PCHIP\big(D_{tr}(\tau)\big),\ \ where\ |\tau| = N = M$$
$$D_n \approx \frac{1}{N}\sum_{\tau=1}^{N} D_{tr}^{pchip}(\tau) \tag{9}$$

To validate our approach, we generated 10,000 independent and identically distributed (i.i.d.) Gaussian signal pairs, each sampled from a standard normal distribution $\mathcal{N}(0,1)$. Calculating the percentage relative difference between the nDTW and the average time-resolved nDTW yielded a median percentage difference of 0.20% (Supplementary Material).

This methodology ensures that the time-resolved metric retains its temporal dynamics and derivative continuity while standardizing its length. Consequently, preserving D_n within the time-resolved measure maintains its reliability, thereby enhancing the robustness of our analysis.

4.4. Resting-state fMRI data

The first dataset used is from the Function Biomedical Informatics Research Network (fBIRN) study including resting fMRI data collected from schizophrenia patients and controls[63]. Scans were collected at a repetition time (TR) of 2 seconds. The study led to a total of 160 controls with an average age of 37.04 ± 10.86 years, ranging from 19 to 59 years. Among these, 45 were female and 115 were male. Additionally, there were 151 patients diagnosed with schizophrenia, with an average age of 38.77 ± 11.63 years, ranging from 18 to 62 years. In this group, 36 were female and 115 were male. The typical controls and schizophrenic patients were meticulously matched in terms of age, gender distribution, and mean framewise displacement during scans (age: $p = 0.18$; gender: $p = 0.39$; mean framewise displacement: $p = 0.97$). Schizophrenic patients were in a clinically stable condition during the time of their scans. The fBIRN dataset is used in all the clinical analysis performed in this study.

The second dataset used in our study is the resting-state fMRI dataset collected from 827 subjects via the Human Connectome Project (HCP) database[64,65]. We utilized both session scans acquired using a Siemens Skyra 3T scanner with a multiband accelerated, gradient-echo echo-planar imaging (EPI) sequence. The scanning parameters were set to a TR of 0.72s, 72 slices, an echo time (TE) of 58ms, and a flip angle of 90°. A voxel size of 2 × 2 × 2 mm was used to acquire 1200 time points of fMRI data for each subject. The HCP dataset was used for our test-retest analysis.

4.5. *Resting-state fMRI pre-processing*

fMRI data requires extensive preprocessing to correct for various sources of noise and artifacts before analysis. The preprocessing steps commonly applied in fMRI studies include slice timing correction, realignment, spatial normalization, and spatial smoothing[66]. Following typical preprocessing[67], we implemented the NeuroMark pipeline, a fully automated spatially constrained ICA on the preprocessed fMRI data[68]. Using the neuromark_fMRI_1.0 template (available in GIFT at http://trendscenter.org/software/gift or http://trendscenter.org/data) we generated 53 intrinsic connectivity networks (ICNs) for each subject. These ICNs are grouped into brain functional domains, including subcortical, auditory, sensorimotor, visual, cognitive control, default mode, and cerebellum.

4.6. *Resting-state fMRI post-processing*

To enhance the quality of these ICNs, we implemented detrending and despiking methods to eliminate drifts, sudden fluctuations, and significant artifacts that may have persisted after the initial preprocessing stages. The time series of the ICNs were bandpass-filtered within two frequency ranges: F1 (0.01-0.198Hz) and F2(0.01-0.15Hz). An infinite impulse response filter was designed using the butter function in MATLAB and applied via the *filtfilt* function to ensure zero phase shifts and preserve phase information. The optimal filter order was estimated using the *Buttord* function in MATLAB, which returns the lowest order of the Butterworth filter with no more than 3dB ripple in the passband and at least 30dB of attenuation in the stopband. Finally, we performed z-scoring on the ICNs. The MATLAB version used was MATLAB R2022a for all steps of the analysis.

4.7. *Test-retest reliability*

Typically, test-retest reliability is evaluated using the intra-class correlation coefficient (ICC). However, the ICC relies on a linear parametric ANOVA model that assumes separability and additivity[69]. This makes ICC unsuitable for DTW applications, as DTW generates a distance metric based on nonlinear warping, where pairwise distances are interdependent[20,21] and thus lack decomposable variance components. We utilize the HCP dataset, which includes two sessions and a large sample size of 827 subjects, facilitating robust test-retest analysis.

4.7.1. *Within-subject variability*

We adopt the approach of a previous study by employing a straightforward method to assess within-subject variability: a paired sample t-test between sessions for each brain network pair[21]. The absolute t-value is reported as a measure of how much the differences between the two sessions deviate from zero, where lower absolute t-values indicate higher within-subject consistency. The formula for calculating the absolute t-value between two sessions of a single network pair across all subjects is provided below:

$$|t|_{within} = \left| \frac{\bar{d}}{s_d/\sqrt{n}} \right| \qquad (10)$$

Where $\bar{d}$ is the mean difference between two sessions, s_d is the standard deviation of the differences, and n is the total number of subjects.

4.7.2. Between-subject variability

To assess between-subject variability, we developed a non-parametric equivalent of the absolute t-value. First, we calculate the differences between the means of each subject's distribution to capture variability across the group. Since the direction of these differences is not of primary interest, we take their absolute values, resulting in a distribution skewed toward zero. This transformation allows us to perform a non-parametric test to evaluate how a non-parametric central tendency measure, such as the median deviates from zero. Unlike the parametric approach, which scales the central tendency measure by the standard deviation, our non-parametric method scales it by the interquartile range to account for the skewed distribution. The formula for the non-parametric absolute variability measure for a single session is as follows:

$$d_i = |s_{1,i} - \bar{s_1}|$$
$$|t|_{between} = \left| \frac{median(d)}{IQR(d)/\sqrt{n}} \right| \qquad (11)$$

Where d_i is the absolute difference between subject i's measure in session 1 ($s_{1,i}$) and the group mean for session 1 ($\bar{s_1}$), $IQR(d)$ is the interquartile range of the differences d, and n is the total number of subjects.

This non-parametric approach provides a robust measure of between-subject variability that is less influenced by outliers and non-normal distributions, thereby enhancing the reliability of our variability assessments.

4.7.3. Composite test-retest reliability score

To further summarize these two approaches to give a wholistic view of test-retest reliability, we compute a composite score of test-retest as follows:

$$trt = 1 - \frac{|t|_{within}}{|t|_{between}} \qquad (12)$$

Scores approaching 1 indicate higher test-retest reliability.

In our study, we compared trt scores across various gamma values of nDTW against correlation as a benchmark. To achieve this, we ranked the trt scores and performed Wilcoxon signed-rank tests between each gamma value's trt scores and the correlation benchmark across all brain network pairs, following a critical difference computation approach.

4.8. Group difference and clinical association analyses

We employed generalized linear models for both group difference analyses and associations with clinical scores. All GLM analyses controlled for sex, age, site, and mean frame displacement. P-values were adjusted using the false discovery rate method, with significance set at a threshold of 0.05. For group difference analyses and computerized multiphasic interactive neurocognitive system scores, a normal distribution was assumed, whereas a Poisson distribution was applied for PANSS score associations due to the positive integer and skewed nature of the fBIRN dataset's PANSS scores. Effect sizes were calculated using Cohen's d.

4.9. Group difference sensitivity test

To evaluate the sensitivity of various gamma values of nDTW and correlation in distinguishing between controls and individuals with schizophrenia, we conducted McNemar's sensitivity tests comparing each gamma value and correlation against each other. Following the GLM group difference analyses, we counted the number of significant brain network pairs (FDR corrected $p < 0.05$) for each gamma value (nDTW) and for correlation. We then compared the unique and shared significant pairs between each gamma and correlation using McNemar's test, with p-values adjusted via FDR correction across all comparisons.

These sensitivity tests were performed separately for each frequency range, F1 and F2. Additionally, we compared F1 and F2 across all gamma values and correlation metric to assess how transitioning from the lower frequency range F2 to the broader F1 range affects group difference sensitivity.

4.10. Validation of high fMRI frequency results.

High-frequency fMRI signals are vulnerable to various sources of noise and artifacts, including physiological factors like respiratory and cardiac activity, as well as non-neuronal influences such as head motion[70]. Comprehensive preprocessing steps followed by our use of ICA help mitigate these concerns. ICA effectively separates independent components, allowing us to identify and remove artifact-related components from the data. Additionally, we included head motion parameters as covariates in our GLM analyses to ensure that detected group differences in high-frequency signals are not attributable to head motion effects.

We conducted several additional analyses further to validate our findings within the F1 frequency range.

4.10.1. Statistical effects on groups with the inclusion of higher frequency

We aimed to evaluate the impact of transitioning from the F2 to the broader F1 frequency range on both control and schizophrenia groups. Since F1 and F2 comprise the same dataset differentiated only by frequency range, a paired sample t-test was appropriate for this analysis. To validate the use of the paired t-test, we first assessed the normality of nDTW scores for each group between F1 and F2 using the Shapiro-Wilk test, ensuring that t-values were close to 1.

Subsequently, we conducted paired t-tests separately for the control and schizophrenia groups to examine the effects of transitioning from F2 to F1, with p-values adjusted using the FDR correction. Effect sizes for these comparisons were calculated using Cohen's d. Additionally, to highlight the differential impact of transitioning from F2 to F1 between groups, we computed the differences in Cohen's d effect sizes between controls and schizophrenia. This comparison aimed to determine whether the transition to the broader F1 frequency range enhances or diminishes group-specific distinctions.

Furthermore, we identified statistical group differences between schizophrenia and controls that were present in F1 but not in F2 by analyzing the shared and unique significant brain network pairs from our GLM analysis (see Section 3.7). We also highlighted their corresponding effect sizes, demonstrating that significant group differences are more pronounced in the F1 frequency range.

4.10.2. Null hypothesis test

The phase randomization (PR) technique generates surrogate fMRI data by preserving the correlation between brain network pairs[71]. This method is suitable for fMRI null hypothesis testing as it assesses non-stationarity by capturing information beyond linear and static correlations[71]. In our previous study[20], we employed PR to evaluate the statistical relevance of both DTW and nDTW in fMRI data, demonstrating that both metrics rejected the null hypothesis for several brain region pairs. This validation confirms that the DTW and nDTW methods are sensitive to capturing information beyond traditional correlation measures. Since DTW and nDTW are amplitude-sensitive methods and the intrinsic brain network timecourses are z-scored, they likely capture amplitude non-stationarity, potentially providing insights into temporal variations in metabolic energy demands between networks.

In this study, we utilize PR to assess the statistical relevance of nDTW in capturing non-stationary amplitude changes specifically due to the inclusion of higher frequency data (0.15–0.198 Hz). The following steps were followed to generate 1,000 surrogate fMRI datasets:

I. Phase Randomization**:** Apply PR to the F1 frequency range data (0.01–0.198 Hz) to create surrogate data, denoted as Z.

II. Filtering Z: Use the designed filter applied to achieve original F2 fMRI data (see section 3.4.) on Z to extract the 0.01–0.15 Hz frequency range of the surrogate data, resulting in surrogate data Y.

III. Isolating Higher Frequencies: Subtract Y from Z to obtain the surrogate data residual high frequency 0.15–0.198 Hz, denoted as X.

IV. Full surrogate data: Add X to the original F2 fMRI data (0.01–0.15 Hz) to generate surrogate data with phase randomization affecting only the residual 0.15–0.198 Hz frequency range.

This process generates surrogate datasets where randomization impacts solely the residual 0.15–0.198 Hz frequency range. A high-pass filter was not applied to Z to obtain the 0.15–0.198 Hz surrogate data because non-ideal filters will artificially create frequency multiples at the edges (~0.15 Hz).

We performed a Wilcoxon rank-sum test (FDR-corrected $p < 0.05$) to compare nDTW scores from the original fMRI data with those from surrogate data. This test assessed whether the significant brain network pairs distinguishing controls from schizophrenia, identified exclusively in the F1 range, also rejected the null hypothesis.

4.10.3. PANSS association exclusive to F1

We identified significant brain network pairs associated with symptom scores that were exclusive to the F1 frequency range and not present in the F2 range.

4.11. Power imbalance dynamics

4.11.1. Brain state estimation

In time-resolved fMRI studies, k-means clustering is frequently utilized to identify recurring brain states within the temporal dynamics of the data[72]. The DTW algorithm inherently anchors the first and last time points during alignment, potentially introducing bias by disproportionately influencing brain states at the temporal extremes. To mitigate this bias, we excluded the first and last 5 time points from the time-resolved nDTW metrics prior to clustering. This exclusion reduces alignment-induced artifacts, enabling the clustering algorithm to more accurately capture intrinsic transitions between brain states.

We concatenated the time-resolved nDTW metrics from all subjects in the fBIRN dataset into a single feature matrix, where each time point from every subject serves as an individual sample and each brain network pair constitutes a distinct feature. We implemented the k-means algorithm with cluster numbers ranging from 1 to 10, setting the maximum number of iterations to 10,000 and using 20 random initializations to ensure robust convergence. The city-block (Manhattan) distance metric was selected for its demonstrated robustness in handling high-dimensional data[73]. To determine the optimal number of clusters, we generated an elbow plot based on the within-cluster sum of squares (WSS). The optimal cluster number was identified as 3, corresponding to the first significant inflection point in the WSS curve’s first derivative.

4.11.2. Markov chain & stationary distribution

We quantified the transitions between brain states by counting the number of times each subject moved from one state to another and normalizing these counts across each state to construct individual transition probability matrices. This represents the probability of a subject transitioning from one state to another and further provides insights into the

Markov chain of state dynamics. To gain a comprehensive understanding of the general transition patterns independent of specific groups, such as patients and controls, we aggregate the probability transitions across all subjects in the fBIRN dataset.

Furthermore, the stationary distribution of the Markov chain represents the long-term behavior of the system, indicating the proportion of time the system spends in each state once it has converged to equilibrium[74]. This distribution serves as an indication of a "stable point" when analyzing systems from the perspective of their Markov chains rather than traditional state-space representations. For the stationary distribution to be unique and ensure convergence from any initial state, the Markov chain must be ergodic[75]. A Markov chain is considered ergodic if it is irreducible (it is possible to get from any state to any other state, aperiodic (the system does not cycle in a fixed pattern), and positive recurrent (the expected return time to each state is finite).

The stationary distribution π is computed by solving the following system of linear equations:

$$\pi P = \pi$$

$$\sum_{k=1}^{K} \pi_k = 1 \qquad (13)$$

Where $\pi = [\pi_1, \pi_2, \dots, \pi_k]$ is the stationary distribution vector, P is the transition probability matrix of the Markov chain, K is the number of distinct states from K-means (3 in our study).

4.11.3. Convergence analysis

How fast a chain takes to reach the stationary distribution gives a similar equivalent meaning to how fast a system takes to reach its stable point from any given state of the system. The spectral gap gives the rate of this convergence to equilibrium[74]. A larger spectral gap implies faster convergence rate to the stationary distribution. It is computed as follows:

$$\gamma_s = \lambda_1 - \lambda_2 \qquad (14)$$

Where λ_1, and λ_2 are the largest and second largest eigen values of the Markov chain respectively. When the chain is ergodic, $\lambda_1 = 1$.

Beyond the spectral gap, the mixing time provides a more comprehensive measure of how quickly the chain approaches equilibrium[74]. The mixing time quantifies the number of steps required for the chain's state distribution to approach the stationary distribution within a specified tolerance level. A prevalent method for determining the mixing time leverages the total variation (TV) distance, which offers a rigorous metric for assessing the divergence between two probability distributions. The total variation distance at time step t is defined as:

$$\|\mu P^t - \pi\|_{TV} = \frac{1}{2}\sum_{k=1}^{K} |\mu P^t(k) - \pi(k)| \qquad (14)$$

Where μ is the initial probability distribution, P^t represents its t-th power of transition matrix, indicating the state probabilities after t transitions, $\pi(k)$ is the stationary probability of state k and K is the total number of distinct states.

The mixing time, denoted as t_{MT}, is the smallest positive integer t for which the TV distance falls below a predefined tolerance level tol:

$$t_{MT} = min\{t \in \mathbb{R}^+ \mid \|\mu P^t - \pi\|_{TV} \leq tol\} \qquad (15)$$

For our analysis, we set the tolerance level to $tol = 10^{-3}$. We also find the mixing time using the initial probability distribution μ farthest from the stationary distribution.

These metrics—spectral gap and mixing time—are instrumental in understanding the dynamic behavior of brain network states. The spectral gap provides insight into the inherent convergence rate of the system, while the mixing time offers a tangible measure of how quickly the system reaches equilibrium. Together, they facilitate a comprehensive analysis of power imbalances and their temporal evolution within the fMRI data, enhancing the robustness and reliability of our findings.

4.11.4. Entropy rate

We investigated how power imbalance dynamics, indicative of the metabolic energy demands between brain networks, inform the flexibility or rigidity of the brain's metabolic consumption by analyzing the entropy rate. The entropy rate is defined as the limit of the average entropy per step as the number of steps approaches infinity. For an ergodic Markov chain, the entropy rate in bits can be mathematically expressed as:

$$H = -\sum_{i=1}^{K} \pi(i) \sum_{j=1}^{K} P(i,j) log_2 P(i,j) \qquad (16)$$

Where $\pi(i)$ is the stationary probability of being in state i and $P(i,j)$ is the transition probability from state i to state j.

The maximum entropy rate for $K = 3$ states is:

$$H_{max} = \log_2(3) = 1.585\ bits \qquad (17)$$

In our study, we present entropy rate as a percentage of H_{max} to enhance interpretability.

The entropy rate provides insight into the balance between order and randomness within the power imbalance dynamics. A low percentage entropy rate indicates strong order in the dynamics, potentially reducing metabolic flexibility. Conversely, a high percentage entropy rate signifies a high degree of randomness, suggesting unpredictable metabolic energy demands between brain networks.

4.11.5. Impact of transition probabilities on Markov chain convergence and entropy rate.

To evaluate how specific transitions within the Markov chain influence the convergence and entropy rates of the dynamics, we systematically perturbed the aggregated transition matrix. This process involved incrementally increasing the probability of individual transition cells and subsequently renormalizing the corresponding rows to ensure that each row's probabilities sum to one. Consequently, the targeted transition's probability increased while the probabilities of other transitions within the same row decreased.

For each perturbed transition, we recalculated both the spectral gap and the entropy rate to determine their percentage relative changes compared to the original values. This perturbation procedure was applied to every transition cell across 10,000 random samples, with perturbation magnitudes ranging from 10^{-1} to 10^{-3} on a logarithmic scale to ensure uniform sampling. To maintain comparability between transitions, each sample employed a single perturbation magnitude uniformly across all transition cells.

4.12. Time-resolved nDTW group difference: schizophrenia vs controls

To assess the clinical relevance of the time-resolved nDTW measure, we conducted group difference analyses on several derived metrics: state transitions, stationary distribution, spectral gap, mixing time, and entropy rate (see Section 3.11). Unlike the aggregated approach in Section 3.11, these metrics were calculated individually for each subject. To ensure the uniqueness of these results, we excluded subjects with non-ergodic state transitions.

Additionally, we included mean dwell time and occupancy rate in our group comparisons. Mean dwell time quantifies the average duration a subject remains in a particular state once entered[76], reflecting the persistence of states within the Markov chain. Occupancy rate represents the percentage of time a subject spends in each state[76], indicating the relative prevalence of states during the observation period.

Using these subject-specific metrics, we distinguished schizophrenia patients from control subjects and performed group difference analyses employing a GLM, as described in Section 3.8. FDR correction is applied to each metric across all three identified states.

4.13. CMINDS score association

Similarly, we employed a GLM, as detailed in Section 3.8, to assess associations between each metric and CMINDS scores—including speed of processing, attention vigilance, working memory, verbal learning, visual learning, and reasoning/problem solving—within the fBIRN dataset. To account for potential group effects, separate GLM analyses were conducted for each group. For transition probabilities, we applied FDR correction to control for multiple comparisons across all transitions.

4.14. Directional time-resolved nDTW

The derivation of DTW, nDTW, and our developed time-resolved nDTW focuses on the absolute differences between aligned signal pairs, revealing power imbalances between brain networks. However, using only absolute differences obscures directional information—specifically, it does not indicate which brain network has higher metabolic demand. Understanding this directionality is essential for designing targeted interventions that address specific metabolic flexibilities or rigidities within neural circuits.

To retain directional information, we modified the time-resolved nDTW by modulating it with directional information, resulting in directional time-resolved nDTW:

$$D_{tr}^{d}(\tau) = \boldsymbol{sign}\left(\left|x\left(\varphi_x(\tau)\right)\right| - \left|y\left(\varphi_y(\tau)\right)\right|\right) \times D_{tr}(\tau) \qquad (18)$$

This modification allows us to detect both the magnitude and direction of power imbalances, identifying which brain network exerts greater metabolic demand relative to its counterpart. We then averaged the directional time-resolved nDTW within each identified cluster, enabling the determination of brain networks that consistently display higher or lower power across states. This refined metric provides a more nuanced understanding of metabolic energy demands, offering precise insights to inform interventions aimed at modulating metabolic flexibility or addressing rigidities within specific neural pathways, thereby enhancing the efficacy of clinical treatments.

To evaluate the similarity of directional information across states, we calculated correlations between the directional time-resolved nDTW metrics of each state. Additionally, we performed a Kruskal-Wallis test to determine whether the distributions of directional information differ among the three states. This dual analysis serves as a sanity check, as we anticipate distinct distributions even if their correlations are comparable.

5. DECLARATION OF COMPETING INTEREST.

None.

6. AUTHORS.

Sir-Lord Wiafe: Conceptualization, Formal analysis, Methodology, Visualization, Writing –original draft. **Spencer Kinsey:** Methodology, Validation, Writing – review & editing. **Najme Soleimani:** Validation, Writing – review & editing. **Raymond O. Nsafoa:** Validation, Supervision. **Nigar Khasayeva:** Validation, Writing – review & editing. **Amritha Harikumar:** Validation, Writing – review & editing. **Robyn Miller:** Validation, Methodology, Supervision, Writing – review & editing. **Vince Calhoun:** Funding acquisition, Validation, Methodology, Resources, Supervision, Writing – review & editing.

7. DATA & CODE AVAILABILITY STATEMENT.

The codes for all our analyses in MATLAB language can be accessed through GitHub (study code). The data was not collected by us and was provided in a deidentified manner. The IRB will not allow sharing of data or individual derivatives as a data reuse agreement was not signed by the subjects during the original acquisition.

8. ACKNOWLEDGMENT.

This work was supported by the National Institutes of Health (NIH) grant (R01MH123610) and the National Science Foundation (NSF) grant #2112455.

9. REFERENCES.

1. Rolfe D, Brown GC. Cellular energy utilization and molecular origin of standard metabolic rate in mammals. *Physiological reviews.* 1997;77(3):731-758.
2. Magistretti Pierre J, Allaman I. A Cellular Perspective on Brain Energy Metabolism and Functional Imaging. *Neuron.* 2015;86(4):883-901.
3. Logothetis NK, Pauls J, Augath M, Trinath T, Oeltermann A. Neurophysiological investigation of the basis of the fMRI signal. *nature.* 2001;412(6843):150-157.
4. Raichle ME. Behind the scenes of functional brain imaging: a historical and physiological perspective. *Proceedings of the National Academy of Sciences.* 1998;95(3):765-772.
5. Tomasi D, Wang G-J, Volkow ND. Energetic cost of brain functional connectivity. *Proceedings of the National Academy of Sciences.* 2013;110(33):13642-13647.
6. Buxton RB, Uludağ K, Dubowitz DJ, Liu TT. Modeling the hemodynamic response to brain activation. *Neuroimage.* 2004;23 Suppl 1:S220-233.
7. Golesorkhi M, Gomez-Pilar J, Zilio F, et al. The brain and its time: intrinsic neural timescales are key for input processing. *Communications Biology.* 2021;4(1):970.
8. Zang YF, He Y, Zhu CZ, et al. Altered baseline brain activity in children with ADHD revealed by resting-state functional MRI. *Brain Dev.* 2007;29(2):83-91.
9. Zou QH, Zhu CZ, Yang Y, et al. An improved approach to detection of amplitude of low-frequency fluctuation (ALFF) for resting-state fMRI: fractional ALFF. *J Neurosci Methods.* 2008;172(1):137-141.
10. Fu Z, Tu Y, Di X, et al. Characterizing dynamic amplitude of low-frequency fluctuation and its relationship with dynamic functional connectivity: An application to schizophrenia. *NeuroImage.* 2018;180:619-631.
11. Allen EA, Damaraju E, Plis SM, Erhardt EB, Eichele T, Calhoun VD. Tracking whole-brain connectivity dynamics in the resting state. *Cereb Cortex.* 2014;24(3):663-676.
12. Zhang G, Cai B, Zhang A, et al. Estimating Dynamic Functional Brain Connectivity With a Sparse Hidden Markov Model. *IEEE Trans Med Imaging.* 2020;39(2):488-498.
13. Wiafe S-L, Asante NO, Calhoun VD, Faghiri A. Studying time-resolved functional connectivity via communication theory: on the complementary nature of phase synchronization and sliding window Pearson correlation. *bioRxiv.* 2024:2024.2006. 2012.598720.
14. Chang C, Glover GH. Time–frequency dynamics of resting-state brain connectivity measured with fMRI. *NeuroImage.* 2010;50(1):81-98.

15. Mitra A, Snyder AZ, Hacker CD, Raichle ME. Lag structure in resting-state fMRI. *J Neurophysiol.* 2014;111(11):2374-2391.
16. Thapaliya B, Akbas E, Chen J, et al. Brain networks and intelligence: A graph neural network based approach to resting state fmri data. *Medical Image Analysis.* 2025;101:103433.
17. Thapaliya B, Wu Z, Sapkota R, et al. Graph-based deep learning models in the prediction of early-stage Alzheimers. Paper presented at: 2024 46th Annual International Conference of the IEEE Engineering in Medicine and Biology Society (EMBC)2024.
18. Thapaliya B, Miller R, Chen J, et al. DSAM: A deep learning framework for analyzing temporal and spatial dynamics in brain networks. *Medical Image Analysis.* 2025:103462.
19. Sakoe H, Chiba S. Dynamic programming algorithm optimization for spoken word recognition. *IEEE Transactions on Acoustics, Speech, and Signal Processing.* 1978;26(1):43-49.
20. Wiafe S-L, Kinsey S, Iraji A, Miller R, Calhoun VD. Normalized Dynamic Time Warping Increases Sensitivity In Differentiating Functional Network Connectivity In Schizophrenia. *bioRxiv.* 2024:2024.2010.2031.621415.
21. Meszlényi RJ, Hermann P, Buza K, Gál V, Vidnyánszky Z. Resting State fMRI Functional Connectivity Analysis Using Dynamic Time Warping. *Frontiers in Neuroscience.* 2017;11.
22. Linke AC, Mash LE, Fong CH, et al. Dynamic time warping outperforms Pearson correlation in detecting atypical functional connectivity in autism spectrum disorders. *NeuroImage.* 2020;223:117383.
23. Wiafe S-L, Faghiri A, Fu Z, Miller R, Calhoun V. *Capturing Stretching and Shrinking of Inter-Network Temporal Coupling in FMRI Via WARP Elasticity.* 2024.
24. Wiafe S-L, Faghiri A, Fu Z, Miller R, Preda A, Calhoun VD. The dynamics of dynamic time warping in fMRI data: a method to capture inter-network stretching and shrinking via warp elasticity. *Imaging Neuroscience.* 2024.
25. Herrmann M, Tan CW, Webb GI. Parameterizing the cost function of dynamic time warping with application to time series classification. *Data Mining and Knowledge Discovery.* 2023;37(5):2024-2045.
26. Fukunaga M, Horovitz SG, de Zwart JA, et al. Metabolic origin of BOLD signal fluctuations in the absence of stimuli. *J Cereb Blood Flow Metab.* 2008;28(7):1377-1387.
27. Roosterman D, Cottrell GS. The two-cell model of glucose metabolism: a hypothesis of schizophrenia. *Molecular Psychiatry.* 2021;26(6):1738-1747.
28. Sarnyai Z, Ben-Shachar D. Schizophrenia, a disease of impaired dynamic metabolic flexibility: A new mechanistic framework. *Psychiatry Research.* 2024;342:116220.
29. Helaly AMN, Ghorab D. Schizophrenia as metabolic disease. What are the causes? *Metab Brain Dis.* 2023;38(3):795-804.
30. Gohel SR, Biswal BB. Functional integration between brain regions at rest occurs in multiple-frequency bands. *Brain Connect.* 2015;5(1):23-34.
31. Birn RM, Cornejo MD, Molloy EK, et al. The influence of physiological noise correction on test-retest reliability of resting-state functional connectivity. *Brain Connect.* 2014;4(7):511-522.
32. Lindauer U, Leithner C, Kaasch H, et al. Neurovascular coupling in rat brain operates independent of hemoglobin deoxygenation. *Journal of cerebral blood flow & metabolism.* 2010;30(4):757-768.
33. Wolf T, Lindauer U, Villringer A, Dirnagl U. Excessive oxygen or glucose supply does not alter the blood flow response to somatosensory stimulation or spreading depression in rats. *Brain research.* 1997;761(2):290-299.
34. Brown AM, Ransom BR. Astrocyte glycogen and brain energy metabolism. *Glia.* 2007;55(12):1263-1271.
35. Pellerin L, Bouzier-Sore AK, Aubert A, et al. Activity-dependent regulation of energy metabolism by astrocytes: an update. *Glia.* 2007;55(12):1251-1262.

36. Hillman EM. Coupling mechanism and significance of the BOLD signal: a status report. *Annu Rev Neurosci.* 2014;37:161-181.
37. Dwyer DS, Bradley RJ, Kablinger AS, Freeman AM, 3rd. Glucose metabolism in relation to schizophrenia and antipsychotic drug treatment. *Ann Clin Psychiatry.* 2001;13(2):103-113.
38. Newcomer JW, Haupt DW, Fucetola R, et al. Abnormalities in Glucose Regulation During Antipsychotic Treatment of Schizophrenia. *Archives of General Psychiatry.* 2002;59(4):337-345.
39. Gatti D, Rinaldi L, Ferreri L, Vecchi T. The Human Cerebellum as a Hub of the Predictive Brain. *Brain Sci.* 2021;11(11).
40. Schmahmann JD. An emerging concept: the cerebellar contribution to higher function. *Archives of neurology.* 1991;48(11):1178-1187.
41. Andreasen NC, Paradiso S, O'Leary DS. “Cognitive dysmetria” as an integrative theory of schizophrenia: a dysfunction in cortical-subcortical-cerebellar circuitry? *Schizophrenia bulletin.* 1998;24(2):203-218.
42. Speers LJ, Bilkey DK. Maladaptive explore/exploit trade-offs in schizophrenia. *Trends in Neurosciences.* 2023;46(5):341-354.
43. Millan MJ, Fone K, Steckler T, Horan WP. Negative symptoms of schizophrenia: Clinical characteristics, pathophysiological substrates, experimental models and prospects for improved treatment. *European Neuropsychopharmacology.* 2014;24(5):645-692.
44. Gu X, Ke S, Wang Q, et al. Energy metabolism in major depressive disorder: Recent advances from omics technologies and imaging. *Biomedicine & Pharmacotherapy.* 2021;141:111869.
45. Meng F, Wang J, Wang L, Zou W. Glucose metabolism impairment in major depressive disorder. *Brain Research Bulletin.* 2025;221:111191.
46. Wu Q, Long Y, Peng X, et al. Prefrontal cortical dopamine deficit may cause impaired glucose metabolism in schizophrenia. *Translational Psychiatry.* 2024;14(1):79.
47. Biswal B, Yetkin FZ, Haughton VM, Hyde JS. Functional connectivity in the motor cortex of resting human brain using echo-planar MRI. *Magn Reson Med.* 1995;34(4):537-541.
48. DeRamus T, Faghiri A, Iraji A, et al. Modular and state-relevant functional network connectivity in high-frequency eyes open vs eyes closed resting fMRI data. *Journal of Neuroscience Methods.* 2021;358:109202.
49. Faghiri A, Iraji A, Damaraju E, Turner J, Calhoun VD. A unified approach for characterizing static/dynamic connectivity frequency profiles using filter banks. *Network Neuroscience.* 2021;5(1):56-82.
50. Jamadar SD, Behler A, Deery H, Breakspear M. The metabolic costs of cognition. *Trends in Cognitive Sciences.*
51. Gonder-Frederick LA, Zrebiec JF, Bauchowitz AU, et al. Cognitive function is disrupted by both hypo- and hyperglycemia in school-aged children with type 1 diabetes: a field study. *Diabetes Care.* 2009;32(6):1001-1006.
52. Cocchi L, Gollo LL, Zalesky A, Breakspear M. Criticality in the brain: A synthesis of neurobiology, models and cognition. *Progress in Neurobiology.* 2017;158:132-152.
53. Moretti P, Muñoz MA. Griffiths phases and the stretching of criticality in brain networks. *Nature communications.* 2013;4(1):2521.
54. Shi J, Kirihara K, Tada M, et al. Criticality in the Healthy Brain. *Front Netw Physiol.* 2021;1:755685.
55. Carhart-Harris RL. The entropic brain - revisited. *Neuropharmacology.* 2018;142:167-178.
56. Xu L, Feng J, Yu L. Avalanche criticality in individuals, fluid intelligence, and working memory. *Hum Brain Mapp.* 2022;43(8):2534-2553.
57. Roheger M, Kessler J, Kalbe E. Structured Cognitive Training Yields Best Results in Healthy Older Adults, and Their ApoE4 State and Baseline Cognitive Level Predict Training Benefits. *Cogn Behav Neurol.* 2019;32(2):76-86.

58. Friston KJ. The disconnection hypothesis. *Schizophrenia research.* 1998;30(2):115-125.
59. Paliwal KK, Agarwal A, Sinha SS. A modification over Sakoe and Chiba's dynamic time warping algorithm for isolated word recognition. *Signal Processing.* 1982;4(4):329-333.
60. Berndt DJ, Clifford J. Using Dynamic Time Warping to Find Patterns in Time Series. Paper presented at: KDD Workshop1994.
61. Faghiri A, Yang K, Ishizuka K, Sawa A, Adali T, Calhoun V. *Frequency modulation increases the specificity of time-resolved connectivity: A resting-state fMRI study.* 2023.
62. Fritsch FN, Carlson RE. Monotone piecewise cubic interpolation. *SIAM Journal on Numerical Analysis.* 1980;17(2):238-246.
63. Keator DB, van Erp TGM, Turner JA, et al. The Function Biomedical Informatics Research Network Data Repository. *Neuroimage.* 2016;124(Pt B):1074-1079.
64. Van Essen DC, Smith SM, Barch DM, Behrens TEJ, Yacoub E, Ugurbil K. The WU-Minn Human Connectome Project: An overview. *NeuroImage.* 2013;80:62-79.
65. Van Essen DC, Ugurbil K, Auerbach E, et al. The Human Connectome Project: a data acquisition perspective. *Neuroimage.* 2012;62(4):2222-2231.
66. Penny WD, Friston KJ, Ashburner JT, Kiebel SJ, Nichols TE. *Statistical parametric mapping: the analysis of functional brain images.* Elsevier; 2011.
67. Fu Z, Batta I, Wu L, et al. Searching Reproducible Brain Features using NeuroMark: Templates for Different Age Populations and Imaging Modalities. *Neuroimage.* 2024;292:120617.
68. Du Y, Fu Z, Sui J, et al. NeuroMark: An automated and adaptive ICA based pipeline to identify reproducible fMRI markers of brain disorders. *Neuroimage Clin.* 2020;28:102375.
69. Wang Z, Bridgeford E, Wang S, Vogelstein JT, Caffo B. Statistical analysis of data repeatability measures. *International Statistical Review.* 2024.
70. Murphy K, Birn RM, Bandettini PA. Resting-state fMRI confounds and cleanup. *Neuroimage.* 2013;80:349-359.
71. Liégeois R, Yeo BTT, Van De Ville D. Interpreting null models of resting-state functional MRI dynamics: not throwing the model out with the hypothesis. *NeuroImage.* 2021;243:118518.
72. Damaraju E, Allen EA, Belger A, et al. Dynamic functional connectivity analysis reveals transient states of dysconnectivity in schizophrenia. *NeuroImage: Clinical.* 2014;5:298-308.
73. Aggarwal CC, Hinneburg A, Keim DA. On the surprising behavior of distance metrics in high dimensional space. Paper presented at: Database Theory—ICDT 2001: 8th International Conference London, UK, January 4–6, 2001 Proceedings 82001.
74. Levin DA, Peres Y. *Markov chains and mixing times.* Vol 107: American Mathematical Soc.; 2017.
75. Basharin GP, Langville AN, Naumov VA. The life and work of A.A. Markov. *Linear Algebra and its Applications.* 2004;386:3-26.
76. Iraji A, Faghiri A, Lewis N, Fu Z, Rachakonda S, Calhoun VD. Tools of the trade: estimating time-varying connectivity patterns from fMRI data. *Social Cognitive and Affective Neuroscience.* 2020;16(8):849-874.